Nanoscale Horizons

ROYAL SOCIETY OF CHEMISTRY

COMMUNICATION

View Article Online
View Journal

Cite this: DOI: 10.1039/d5nh00788g

Received 3rd December 2025,
Accepted 18th February 2026

DOI: 10.1039/d5nh00788g

rsc.li/nanoscale-horizons

DNA nanostars that self-assemble into core–shell condensate microdroplets

Karuna Skipper [ab] and Shelley F. J. Wickham *[abc]

Phase-separating DNA condensates have a range of potential uses, from synthetic cells to microreactors, uniquely combining programmable nanoscale subunits with tuneable microscale properties. However, DNA condensates are inherently unstable, leading to dynamic heterogeneity and uncontrolled mixing, limiting their ability to control complex reaction pathways. Here, we develop multi-layered DNA condensate 'droplets' composed of DNA nanostars, where nanostars with different DNA sequences form distinct core and shell regions. Nanostar properties were first explored to understand how structural changes in geometry, valency, and interaction strength affect droplet phase-separation temperature, size, stability, and permeability. We show that when pairs of nanostars self-assemble in the same solution, the order of phase-separation determines core or shell destination, whereas the proportion of surfactant nanostars that link the two populations determines shell morphology. Testing 50 different nanostar combinations, we found that membrane-like systems, where the shell fully encloses the core, form if the difference in phase-separation temperatures of the two nanostars is greater than 3 °C with 16–25% surfactant nanostars. For 3 different core nanostars, we demonstrate a range of shell nanostars with different material properties and morphologies. Core–shell droplets have well-defined size, stability over time, and core permeability is controlled by shell properties. Furthermore, droplet size and membrane thickness were controlled by adjusting the thermal annealing rate during assembly. These techniques provide a diverse library of droplets suitable to be used as microscale reaction compartments, with predictable size, mono-dispersity, membrane thickness, and permeability. We envision that core–shell DNA nanostar droplets will open new avenues for assembling programmable materials that combine DNA condensates with DNA molecular circuits, exploiting cell-like properties such as compartmentalisation and controlled transport to achieve programmable synthetic micro reactors.

New concepts

Synthetic phase-separated liquid condensates capable of forming microreactors have potential for diverse applications, from controlling multi-step reaction pathways to building synthetic cells with emergent properties. We use DNA nanostars to assembly microscale DNA condensate droplets with complex microarchitectures, including core–shell droplets. By tuning the physical structure and interaction strength of nanoscale components, we achieve DNA condensates with a range of physical and chemical properties, such as tuneable viscosity and permeability.A notable feature of our system is our demonstration that interaction strength determines which nanostar type forms the core, allowing us to design multi-phase droplets with programmable physical properties in specific regions. We further show that core-shell systems can have a range of cell-like properties that are also useful for nano and microreactors, such as well-controlled size, enhanced uniformity, and stability over time. Notably, our technique relies solely on canonical DNA base pair interactions, meaning all the specificity and dynamic control of DNA computing and chemical reaction networks can be exploited in these synthetic systems.

Introduction

Liquid–liquid phase separation (LLPS) occurs when dissolved solutes demix into molecule-rich and molecule-poor regions and plays a key role in cell physiology.[1–3] Molecule-rich regions, also known as condensates, coacervates, or droplets, can act as liquid-like membraneless organelles and contribute to cell processes from germ cell maintenance to apoptosis. The formation of condensate droplets is driven by multivalent interactions between biomolecules and results in densely packed regions with higher biochemical reaction rates, selectively enhancing or inhibiting cellular processes. LLPS has also been used to form macromolecular condensates in synthetic systems, including peptides,[4,5] polymers,[6–11] and DNA,[12–23] providing insight into cellular functions and developing new materials, such as synthetic microreactors.[6,24–26] Spatial organisation of chemical and biomolecular interactions into chains of microreactors can be used to

[a] School of Chemistry, The University of Sydney, Sydney, NSW 2006, Australia. E-mail: shelley.wickham@sydney.edu.au
[b] The University of Sydney Nano Institute, The University of Sydney, Sydney, NSW 2006, Australia
[c] School of Physics, The University of Sydney, Sydney, NSW 2006, Australia

control reaction pathways and improve low-yield products.[27–29] For example, linking multiple coacervates into larger superstructures can lead to self-directing circuits.[30,31] Engineering the micro-scale architecture and inter-droplet interactions of synthetic coacervates is key to designing microreactor functions.

Recently, synthetic condensates assembled from nucleic acid nanostructures have demonstrated dynamic programmable properties.[12,13,15,17,18,31–37] DNA hybridisation allows for design of nanostructures with controlled size and valency, forming a branched motif called a DNA 'nanostar' (NS). DNA nanostars have been shown to undergo liquid–liquid phase separation and form microscale condensate droplets through multi-valent interactions between short single-stranded DNA (ssDNA) domains that are self-complementary, known as 'sticky ends' (SE). An advantage of DNA is that nanostar structure and sequence variants may be easily synthesised and rapidly prototyped to vary droplet size, homogeneity, density, and viscosity.[18,32] Physically similar nanostars with 'orthogonal' (non-interacting) DNA sequences can be designed to be immiscible while maintaining similar physical properties.[17] Furthermore, DNA strand displacement reactions, where a partially complementary DNA duplex is displaced by a fully complementary 'invader' strand, allow for dynamic and programmable systems.[38] For example, triggering release and transfer of guest molecules in condensates.[11] DNA nanostar droplets have been developed as microreactors, demonstrating triggered mixing and demixing of droplets,[17] selective cargo capture,[16] and enhancement of reaction rates.[30,35]

A current limitation of DNA nanostar condensates for use as microreactors is that LLPS systems are inherently unstable, with dynamic fusion and rapid exchange of components with solution.[18,39] In contrast, living cells achieve sophisticated spatial control of reactions in stable compartments with selective transport across semipermeable membranes, enabling complex emergent behaviours such as evolution and chemotaxis.[39] When nanostar condensates are thermally annealed, droplets grow *via* fusion and ripening over time, leading to highly polydisperse populations.[18,40] Polydispersity in size leads to variation of diffusion rates and amount of captured reagents, resulting in a nonuniform population of microreactors. Uncontrolled fusion or transfer of contents between distinct droplet components in a multi-droplet pathway results in content mixing, resulting in loss of spatial organisation and function. Surface passivation of condensates by coating[5,6] or capping[41] has been shown to reduce droplet-droplet fusion while still allowing the movement of reagents, products, and waste material, increasing complexity in microreactor systems.[37,40] However, such approaches often involve the use of non-DNA nanostar components, such as cholesterol, lipids, or purine motifs, reducing the multiplexing and programmability provided by DNA nanostar condensates.

The key challenge in building DNA droplet microreactors is to achieve uniform populations of DNA nanostar compartments that remain stable as distinct populations when mixed, but can also be programmably triggered to achieve dynamic interactions. Here, we address the challenge of balancing stability and dynamic properties by designing core–shell DNA nanostar microdroplets. First, we demonstrate two-phase DNA nanostar condensates, where two orthogonal nanostar populations are mixed with a small amount of linker, or 'surfactant', nanostars that are complementary to both populations (Fig. 1A and B). We then explore how tuning the difference in phase separation temperature of the two nanostar populations can achieve control of two-phase droplet microarchitecture, producing core–shell droplets (Fig. 1C and D). Next, we compare the physical properties of single-phase and core–shell DNA nanostar droplets, including core size, polydispersity, permeability, stability, and contents transfer in mixed populations (Fig. 1E and F). Overall, core–shell DNA condensates provide new tools for the formation and manipulation of synthetic microreactors.

Results

Single-phase DNA nanostar droplets

First, we characterised the assembly and physical properties of single-phase DNA nanostar droplets using nanostar motifs adapted from previous designs.[16,17,42] Multiple nanostars were designed and characterised to produce a library of nanostars with sufficient diversity of physical properties to produce core–shell droplets with different properties to core-only droplets. Key parameters explored were: arm number (3; 4), arm length ('short', 16 bp, ~5.4 nm; 'long', 23 bp, ~7.7 nm), SE length (6; 8; 10-nt), SE strength ('weak'; 'regular'; 'strong') (SI Table S1-3). Sticky end strength was quantified by the predicted free energy of binding, which is known to depend on the GC content and nearest neighbour stacking in the SE sequence.[43] Notation used for stars is '4L10' for a star with 4-arms, long arm length, SEs of 10-nt length and regular strength. Of total 36 possible nanostars, 15 were compared: 3 structures (3S, 4S, 4L) and 5 SEs (6-nt, 8-nt-weak, 8-nt, 8-nt-strong, 10-nt), with corresponding predicted binding energies ($-\Delta G$ = 6.6, 8.1, 10.9, 11.5, 12.3 kcal/mol). These correspond to SE melting temperatures[44] of (T_M = 31, 34, 49, 52, 54 °C) at 40 μM strand concentration and 0.5 M NaCl. Calculated SE ΔG and T_M are properties of the SE sequence, not the nanostar. The droplet properties depend on the nanostar phase separation temperature (T_{PS}), which is affected by SE properties, nanostar valency and geometry,[17,45] and was experimentally determined in this work using hybridisation curve analysis (HCA) during cooling.[46] All arm sequences and SE variant sequences were designed to be orthogonal and were confirmed to have no cross-interactions by analysis with NUPACK software.[44] All SE sequences were designed to be palindromic.

DNA nanostar droplets have been proposed to assemble in a multi-step process on cooling (Fig. 1C).[17] First, the arm domains bind to form discrete multi-arm stars at the temperature of nanostar formation (T_{NS}). Second, inter-star bonds form *via* SE–SE interactions, initiating phase-separation into liquid droplets at the temperature of phase separation (T_{PS}). Lastly, the system reaches the temperature of gelation (T_G) when the temperature is sufficiently low that the nanostars form a

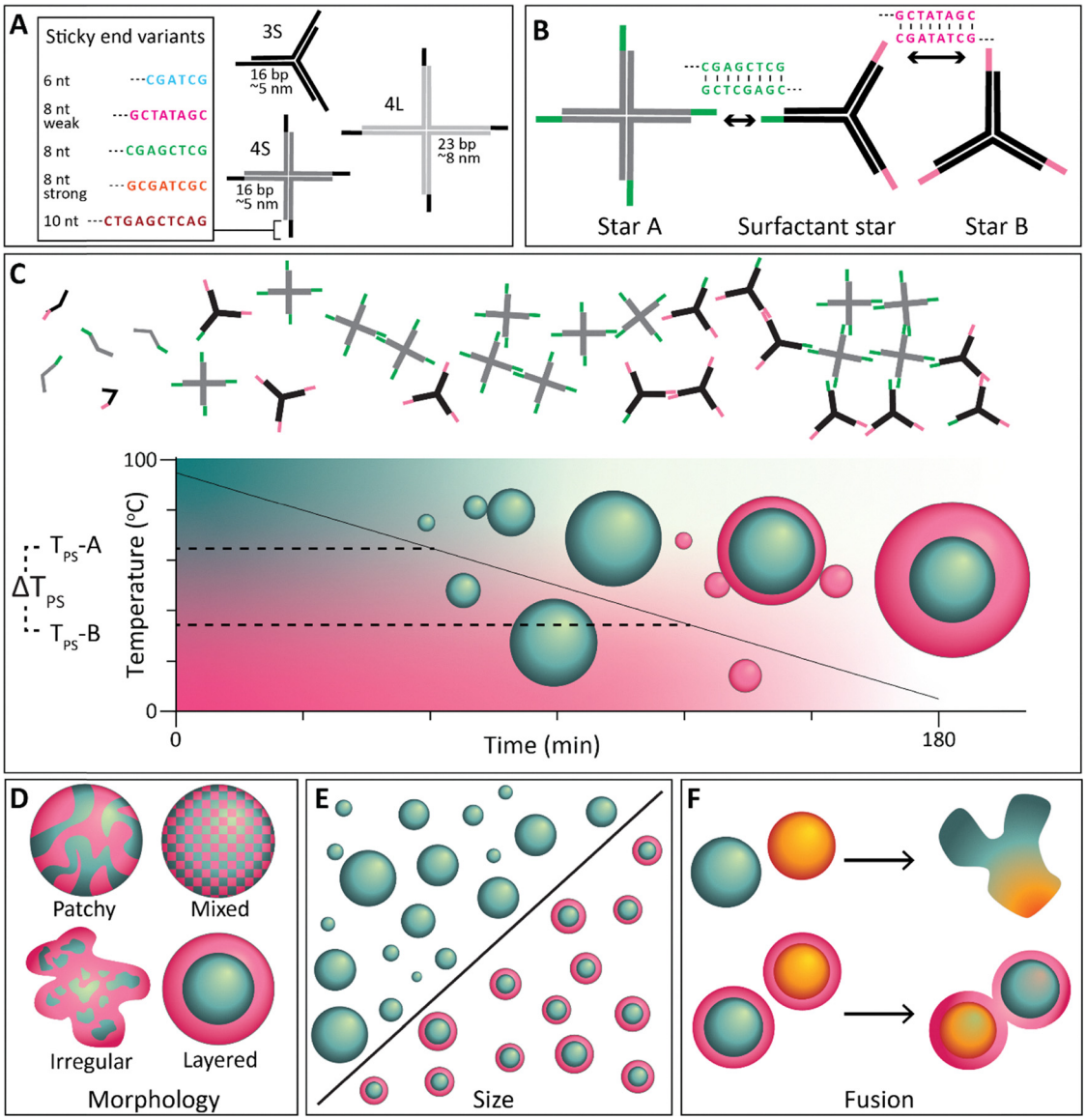

Fig. 1 Multi-phase DNA nanostar condensate droplets. (A) Design of trivalent and tetravalent nanostars (NS) of varying arm length and number, and sticky-end (SE) length and sequence. (B) Design of surfactant stars, which are modified by replacing SEs of one star type with the SE of a second nanostar. The degree of complementarity (%C) gives the total SE replacement across the whole nanostar. (C) Two-phase droplet formation is expected to occur in stages on cooling (left to right). At high temperature (left), all strands are ssDNA. On initial cooling (middle), strands hybridise into three populations of stars (green, pink, green-pink surfactant). Further cooling (right) leads to phase separation of liquid droplets. Green droplets have higher phase separation temperature (T_{PS}) and form first. Surfactant stars can hybridise to the green core, nucleating formation of a pink shell that acts as a kinetic trap, stopping core growth. Shading represents the bulk phase concentration of non-phase separated nanostars. (D) The morphology of a two-phase droplet system is affected by the %C of the surfactant star population and the difference in phase separation temperatures of the two stars. (E) and (F) Encapsulation of the core inside a shell affects homogeneity of core size, fusion of cores, and reduces content transfer between cores.

continuous three-dimensional network. Typically the gel transition is observed by reduced NS mobility in Fluorescence recovery after photobleaching (FRAP) measurements or by increased resistance to deformation.[17,47] T_G for nanostar droplets is known to be above the T_M for SE–SE interactions.[17] The critical temperatures, T_{NS}, T_{PS}, T_G, are known to affect droplet morphology and have been shown to depend on nanostar valency, arm length and sequence, as well as SE length and sequence. The 'active range' for droplets is defined as the period for which the system remains liquid during cooling (T_{PS} to T_G), during which time droplets can grow. For the same thermal annealing ramp different T_{PS} and T_G will result in different length active ranges.[17]

The properties of single-phase droplets were characterised to verify that the range of NS structures selected (SEs, arm lengths, valencies) provided diversity of physical properties (SI) and key results are summarised here. The size and shape of droplets at 0.5 M NaCl were quantified by confocal microscopy at room temperature ($T_R \sim 21$ °C) and found to depend strongly on SE strength, valency, and arm length (Fig. S1–S4).

The trends of single-phase droplet size and deformation across nanostar variants were consistent with previously described results.[13,18,44] Additional molecular-level investigations of single-phase droplets allowed for characterisation of their physical properties. Internal nanostar mobility was qualitatively analysed using FRAP, showing a decrease in fluorescence recovery at 5 minutes from 0.76 to 0.08 AU when increasing SE strength (3S8-W *versus* 3S8-S), and a decrease from 0.76 to 0.31 AU when increasing valency (3S8-W *versus* 4S8-W) (Fig. S6). Partition coefficients of Dextran cargo were found to be affected by nanostar design, with 4S droplets having significantly lower infiltration indicating smaller mesh size than 3S and 4L droplets (Fig. S7 and S8).

Two-phase DNA nanostar droplets

Combinations of two droplet phases were assembled by co-annealing orthogonal nanostars with and without surfactant nanostars. 'Surfactant' nanostars were designed by adding star-A SE sequences to arm domains of star-B, producing a new hybrid star with a mix of SEs (*e.g.* 8-W and 8) to crosslink the two original stars (Fig. 1B). SE replacement was achieved by modification of either one or multiple arms. The resulting surfactant nanostar is described by the 'degree of complementarity' (%C) which is the total % of all star-B SEs replaced with the star-A SE. We note that the degree of complementarity is different to the percentage replacement of individual arms. For example, 25%C for a 4-arm star could be achieved by 100% replacement of 1 arm, 25% replacement of all 4 arms, or many intermediate replacement patterns. Surfactant stars are denoted by original star, replacement SE sequence, and degree of star complementarity: '4L8-S:8 25%' denotes a surfactant version of the 4L8-S star with 25% of 8-nt-S SEs across the whole nanostar replaced with 8-nt SEs.

First, the two extremes of fully immiscible and mixed droplets were tested. Co-annealing of nanostars with entirely orthogonal arm and SE sequences resulted in two separate droplet phases, as expected from previous work[16,17,48] (Fig. 2A(i)). Co-annealing of nanostars with complete SE-complementarity but NS arm orthogonality resulted in fully mixed and uniform droplets for all arm-size combinations, with no evidence of size-based de-mixing of nanostars (Fig. 2A(ii)). In contrast, in previous work combinations of small and large nanostars with sticky ends replaced by cholesterol moieties resulted in de-mixed droplets.[49] This difference suggests that the interaction between complementary SEs may overcome size-based de-mixing or exclusion, whereas cholesterol-induced interactions do not.

Next, partial mixing of orthogonal droplets was tested in an AB nanostar system by replacing a fraction of B-star SEs with A-complementary SEs. As described above, the % complementarity may be achieved with different arm replacement patterns. Replacement patterns were compared for a two phase system (4S8 4L8-strong): 100% SE replacement of 1 arm resulting in all B stars becoming surfactant stars, 50% of 2 adjacent arms resulting in a distribution of B stars with 0–2 SEs replaced, 50% of 2 opposite arms, 25% of all 4 arms resulting in resulting in a distribution of B stars with 0–4 SEs replaced. Interestingly, droplet morphology was observed to be the same for all different arm replacement patterns and was found to depend only on the overall % of SEs replaced (Fig. S9 and S10). Therefore, for the following characterisation 1-arm replacement was used for low % replacement ($<$16% 3-arm, $<$25% 4-arm), while adjacent 2-arm replacement was used for other cases ($>$25%).

Selected two-phase combinations were then investigated by confocal microscopy for 0–50% complementarity (Fig. 2B(i–iii) and Fig. S11–S13). Hybridisation curve analysis (HCA) was used to estimate T_{PS} for one and two-phase droplet systems comparing 0 and 25%C (Fig. 2B and Fig. S14). SE replacement had minimal effect on observed T_{PS} for single phases at low %C values. Co-annealed solutions of two stars had two distinct incidences of phase separation with T_{PS} values corresponding to the two component stars and were indistinguishable for 0 and 25%C. Thus, single-phase T_{PS} HCA values were used to calculate ΔT_{PS} for the two phases and compared to droplet morphology observed in confocal microscopy data.

For all combinations of nanostars at the extremes of SE complementarity, the two phases were either completely distinct (0%C, Pearson correlation coefficient $r < 0$) or mixed (50%C, r = 0.6–0.9) (Fig. 2B). At moderate complementarity, a range of morphologies were observed in order of increasing SE replacement: attached droplets (Fig. 2B(i), 12.5%), followed by patchy droplets, and then layered core–shell droplets (Fig. 2B(ii), 16%). Core–shell droplets occurred for two-phase systems with $\Delta T_{PS} >$ 3 °C, at 16%C for 3-arm B stars and 25%C for 4-arm B stars. For $\Delta T_{PS} < 3$ °C, patchy droplets tended to form at 25%C instead of layered droplets (Fig. 2B(ii) 25%, Fig. S15).

The difference between core–shell and patchy morphologies was defined using analysis of confocal microscope images. Multiple intensity profiles were extracted across the diameter of a single droplet. A core–shell morphology is expected to produce two peaks of similar width and intensity at the edge of the droplet, with these values remaining consistent across different angles of measurement (Fig. S15). Patchy morphologies were defined by lack of radial symmetry.

The changes in droplet morphology observed with increasing SE replacement for a two-phase system with $\Delta T_{PS} \lesssim 3$ °C were similar to those observed in previous works. For example, in a system of two orthogonal stars with the same structure (both 4L6) and therefore similar T_{PS}, surfactant surface wetting was observed at lower % surfactant, then bifacial droplets at 50% surfactant (equivalent to 25% SE complementarity), then mixing.[16] This is similar to results here for the 4L8 4S8-strong system (Fig. 2B(i)), consisting of stars of similar T_{PS}.

For core–shell droplets formed from high ΔT_{PS} NS combinations, the phase with higher T_{PS} formed the core, in agreement with previous work on cholesterol-modified DNA nanostars[22] and poly-purine motif DNA coacervates.[21] The key difference here is that by including a greater range of nanostar structures, it was possible to achieve the larger ΔT_{PS} required to form core–shell droplets in a DNA-only system driven by canonical DNA hybridisation.

A total of fifty different nanostar combinations were tested, varying the arm length, valency, SE sequence, or surfactant phase of the nanostars (Fig. 3 and Fig. S16). Trends in the

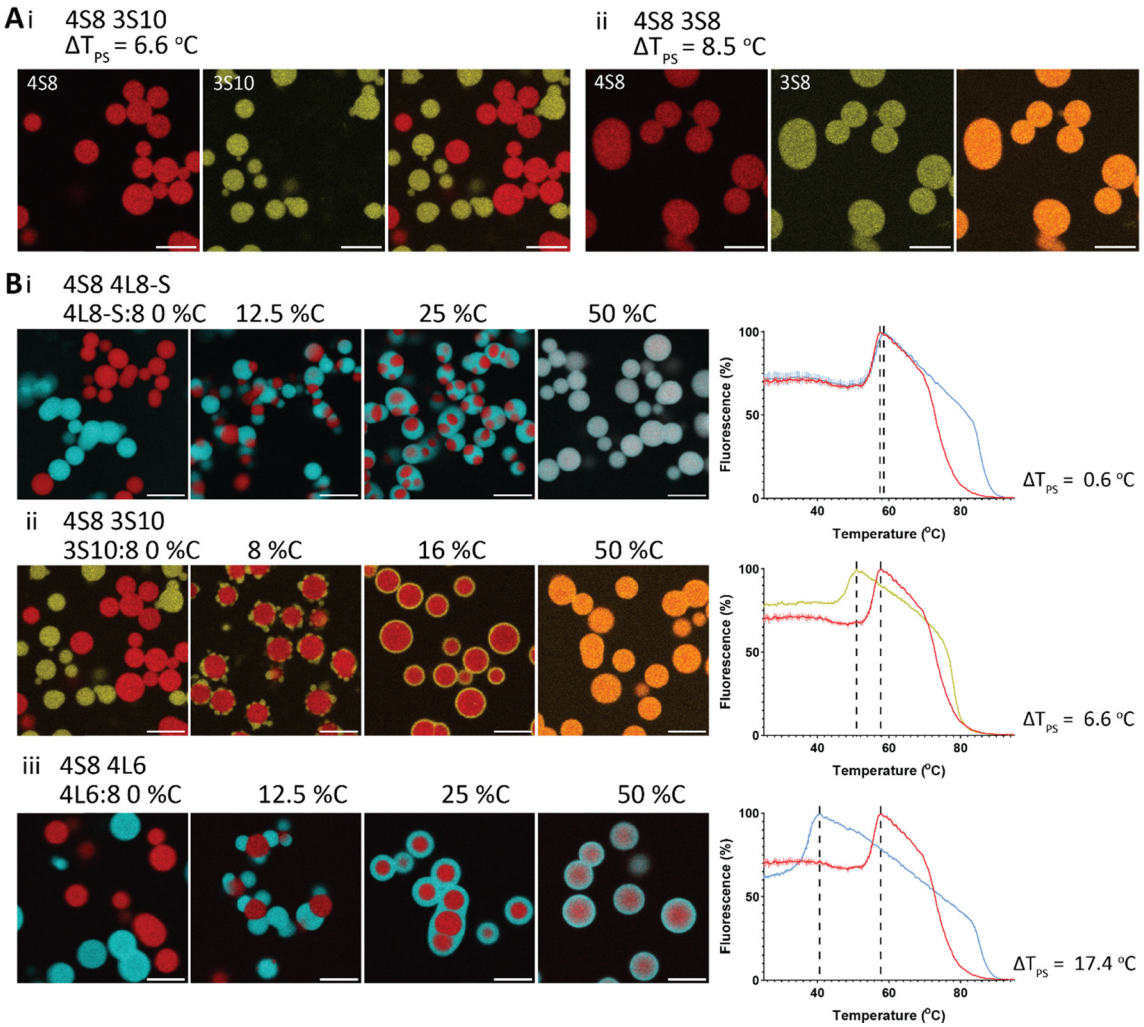

Fig. 2 (A) (i) Nanostars with orthogonal SE and orthogonal arm sequences result in distinct droplet populations. (A) (ii) Nanostars with the same SE sequences and orthogonal arms form mixed droplets. (B) Increasing the degree of interaction between NSs leads to an increase in the degree of wetting between phases. The resulting micro-architecture depends on the difference in phase separation temperatures, with $\Delta T_{PS} < 3$ °C forming patchy droplets, and $\Delta T_{PS} > 3$ °C forming core–shell structures. Right: Hybridisation curves, highlighting onset of phase separation. Scale bars 10 μm.

properties of core–shell droplets were then investigated, including star type, ΔT_{PS}, annealing rate, nanostar size (Fig. S5), core to shell nanostar size difference, shell width, core radius, and total radius (Fig. 4). Firstly, all combinations of nanostars that formed core–shell structures under these conditions had ΔT_{PS} close to or above 3 °C (Fig. 4A). Core–shell structures successfully formed for both core > shell and shell > core NS size combinations. These results suggest that the $\Delta T_{PS} > 3$ °C threshold is a useful indicator of potential core–shell formation for the range of parameters tested. However, this is not a sufficient condition for predicting core–shell structures in all cases, as patchy, irregular and mixed structures were observed for some systems with $\Delta T_{PS} > 3$ °C (Fig. S17), and other parameters such as NS size may contribute to morphology.

In contrast, other work has shown that core–shell formation can occur at high Δ[size] values (arm ratio >1.2; Δ NS size = 5–15 nm; NS size = 19–34 nm) for cholesterol-modified DNA nanostars due to sized-based de-mixing, with the smaller NS forming the core.[47] For comparable NS combinations tested here with the same SE on both stars but different sizes (Fig. 3, yellow boxes), only mixed droplets were observed for all size combinations tested (arm ratio > 1.2; Δ NS size = 4–10 nm; NS size = 12–24 nm). The NS combinations tested here had a similar arm ratio and Δ NS size but a smaller range of NS sizes, compared to the previous study. Thus, size-based demixing of fully SE complementary nanostars into core–shell structures was not observed here, but may still occur for NS combinations with larger absolute size or size differences.

Importantly, core size was significantly decreased for core–shell in comparison to core-only droplets in all systems (ANOVA, $p < 0.0001$ for 4S8 and 4L8 cores, $p < 0.001$ for 4L10 core). Core size polydispersity also decreased for 4S8 and 4L8 cores with a shell (F-test, $p < 0.0001$, Fig. 4D and Fig. S18). For the 4S8 core, three different shells were compared with increasing ΔT_{PS} (3S10, ΔT_{PS} = 8.5 °C, 4L6, ΔT_{PS} = 15.9 °C, 4L8-weak, ΔT_{PS} = 17.1 °C). Here the active range would be expected

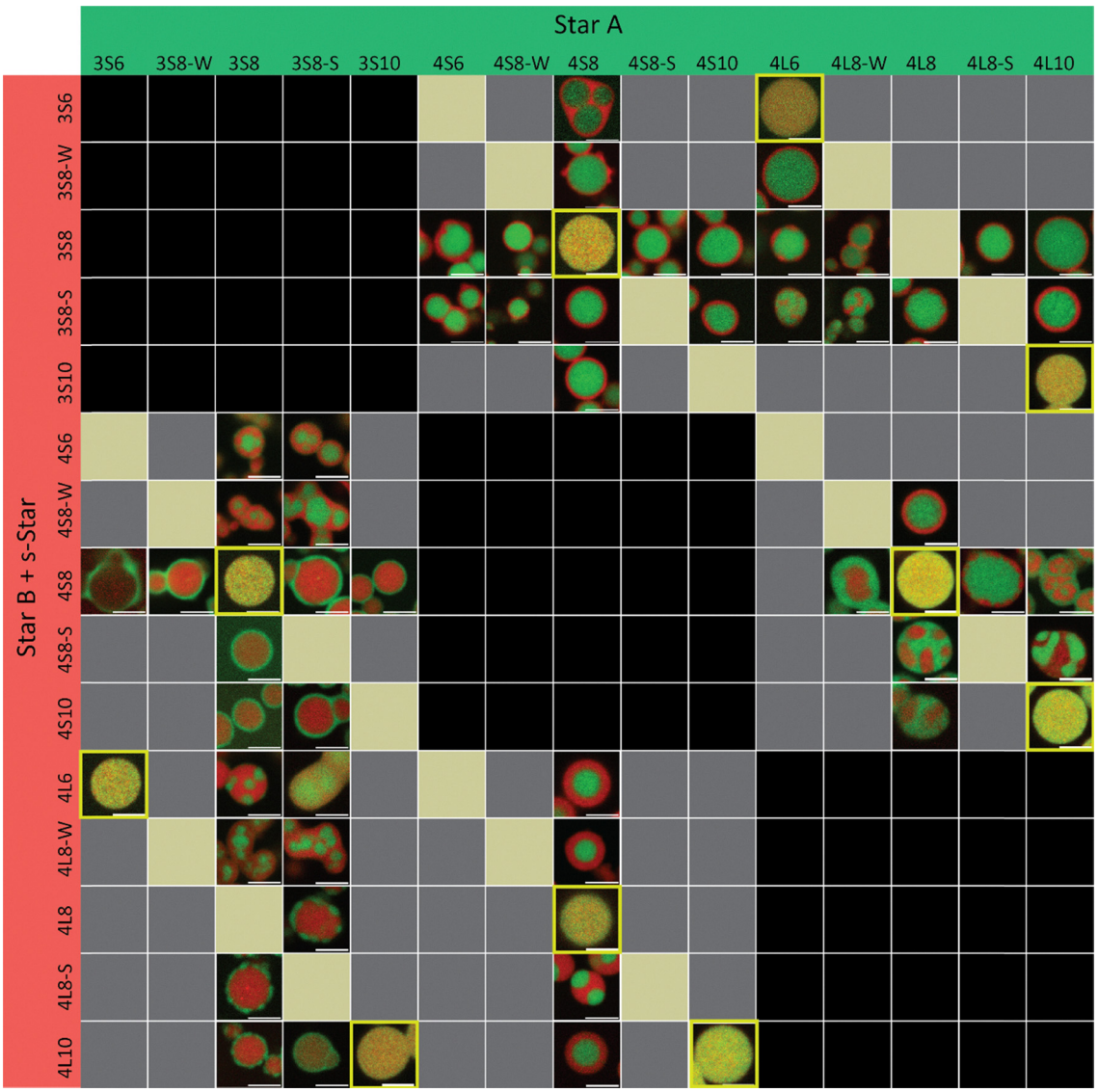

Fig. 3 Comparison of 50 multi-star systems. Fifty pairs of non-complementary SE nanostars were tested. Star A (green) was unmodified; star B (red) includes surfactant stars created by SE replacement, 16%C for trivalent and 25%C for tetravalent. Black squares: nanostars have matching arm sequence and mixed droplets are predicted. Yellow squares: nanostars have complementary SE sequence. Mixed droplets are predicted and were observed for all examples tested. Grey squares are untested combinations. Scale bars 5 μm.

to increase with ΔT_{PS}, and while no significant difference was observed in size, the size distribution for the shell with the smallest active range is significantly smaller (F-test, $p < 0.001$, comparing 3S10 shell to 4L6 or 4L8-weak). For the 4L10 cores no significant effect of the shell was observed on the size distribution of the system. These stars have strong SEs (T_{PS} = 62 °C) and are expected to already have a short active range for the core-only droplet, so addition of the shell likely has a reduced effect. Similarly, increasing annealing rate from −1.0 °C min^{-1} to −5.0 °C min^{-1} resulted in a decrease in both core and total size for core–shell droplets from 3.81 μm ± 0.42 μm to 1.41 μm ± 0.14 μm (Fig. 4E), consistent with previously reported behaviour of single-phase systems.[50]

In contrast, shell width was observed to be consistent across a core–shell population, but varied between different nanostar combinations. Nanostar size was found to have a significant positive correlation with shell thickness (linear regression R^2 = 0.75, slope p-value < 0.0001, Fig. 4C). Shells formed by 4L nanostars were significantly thicker than others, suggesting the longer 4L arm produces a network that fills a larger volume than the shorter arm stars (3S, 4S). The thickness of the shell also decreased with increasing ramp rate for 4S8 4L6 core–shell droplets, observed as an increase in core:total size ratio (Fig. 4E inset), suggesting that the time between the onset of shell formation and the end of phase separation also contributes to shell thickness. Core–shell droplets assembled at very high ramp-rates (−5.0 °C min^{-1}) tended towards 'strings' of multiple conjoined droplets, sharing partially fused shells (Fig. 4E(iv)), indicating an upper bound to rates useful for formation of discrete droplets.

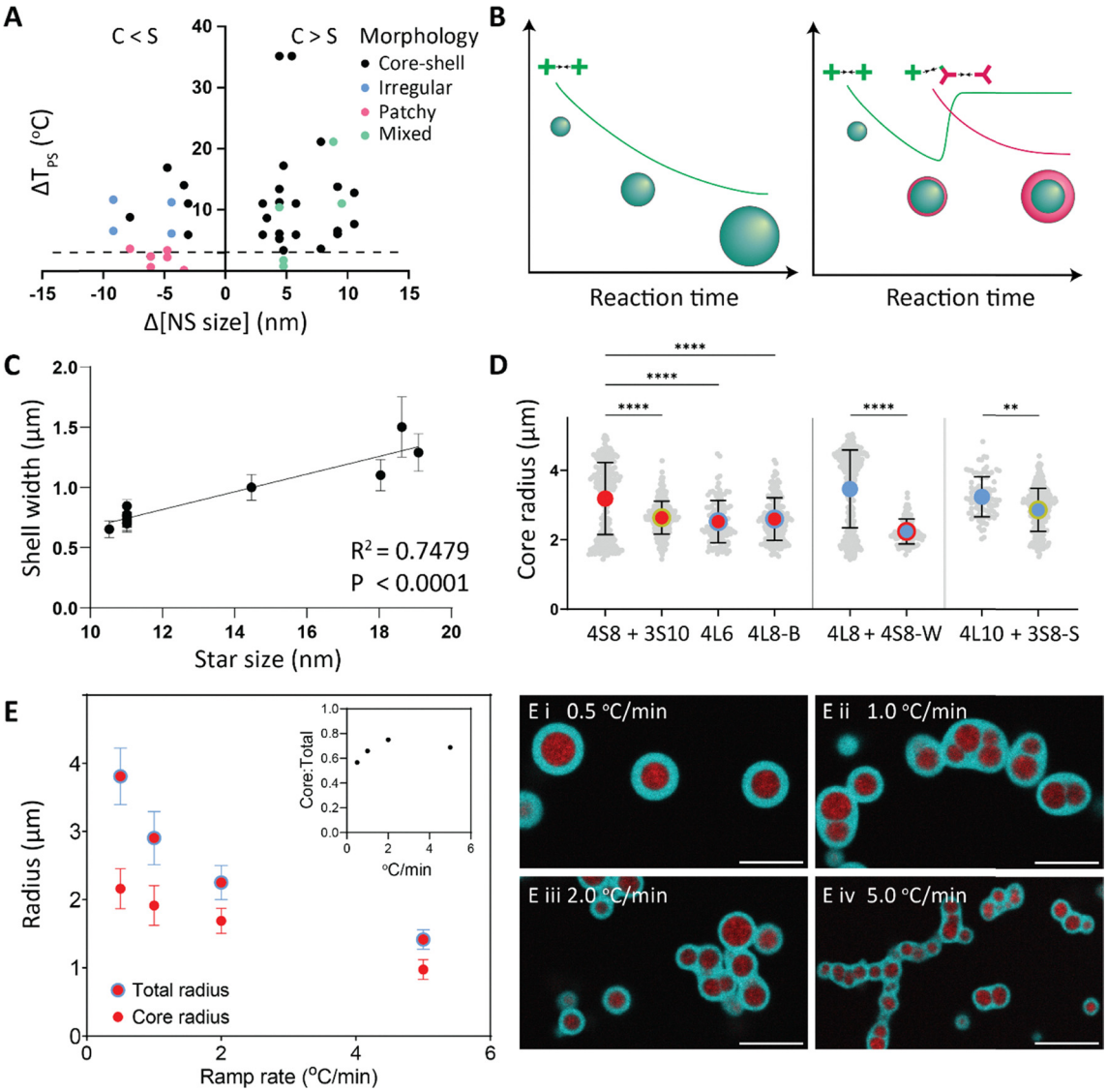

Fig. 4 Trends in core–shell droplet morphology, size, polydispersity and shell thickness. (A) Effect of NS size difference ($S_{high\text{-}T_{PS}} - S_{low\text{-}T_{PS}}$) and ΔT_{PS} on incidence of core–shell (black), irregular (blue), patchy (pink), or mixed (green) structure formation. Horizontal line at 3 °C. (B) Schematic representation of energy profile of bare and core–shell systems. (C) Measured width of droplet shells as a function of shell nanostar size S_G. There is a significant correlation between star size and shell width (R^2 = 0.75, P-value < 0.0001). (D) Mean radii ± SD of core-only and core–shell for 4S8, 4L8, and 4L10 cores. Core–shell droplets are smaller and less polydispersed than core-only (pairwise one-way ANOVA). (E) Faster annealing rates result in smaller and more uniform droplets with proportionally thinner shells (inset, ratio of core to total size). Scale bars 10 μm.

Core–shell DNA droplet stability

Along with well-defined size, model protocells and microreactors also require stability over time. We next compare stability over time for the 4S8 3S10 system at a range of temperatures (4–37 °C, 0–45 h). From single-phase studies, the core-only 4S8 droplets had no recovery in FRAP measurements (Fig. S6) and low deformation at the surface at T_R (Fig. S3). However, after 15 h incubation at 31 °C, significant coalescence of core-only droplets was observed (Fig. 5A and Fig. S19), with complete merging at 34 °C, whereas at 4 °C droplets remained distinct.

In contrast, core–shell droplets remained as distinct populations over longer times (45 h at 31 °C, Fig. S19) and at higher temperatures (15 h at 34 °C, Fig. 5A). Coalescence of core–shell droplets was also qualitatively different to the core-only system and occurred as merging of shells leading to large irregular multi-core structures. The deformation of core–shell droplets was characterised by defining circles around the maximum radius of each droplet, and determining the area of intersection between adjacent droplets (Fig. 5B and Fig. S20). Samples incubated at 34 °C or higher had a significant increase in the area of intersection, indicating increased deformation. The morphology of a core–shell system depends on the three surface tensions (A/dilute, B/dilute, and A/B) in the system,[48] all of which vary with temperature. It is possible that cores within this system may remain as physically distinct compartments at even longer timescales than characterised here.

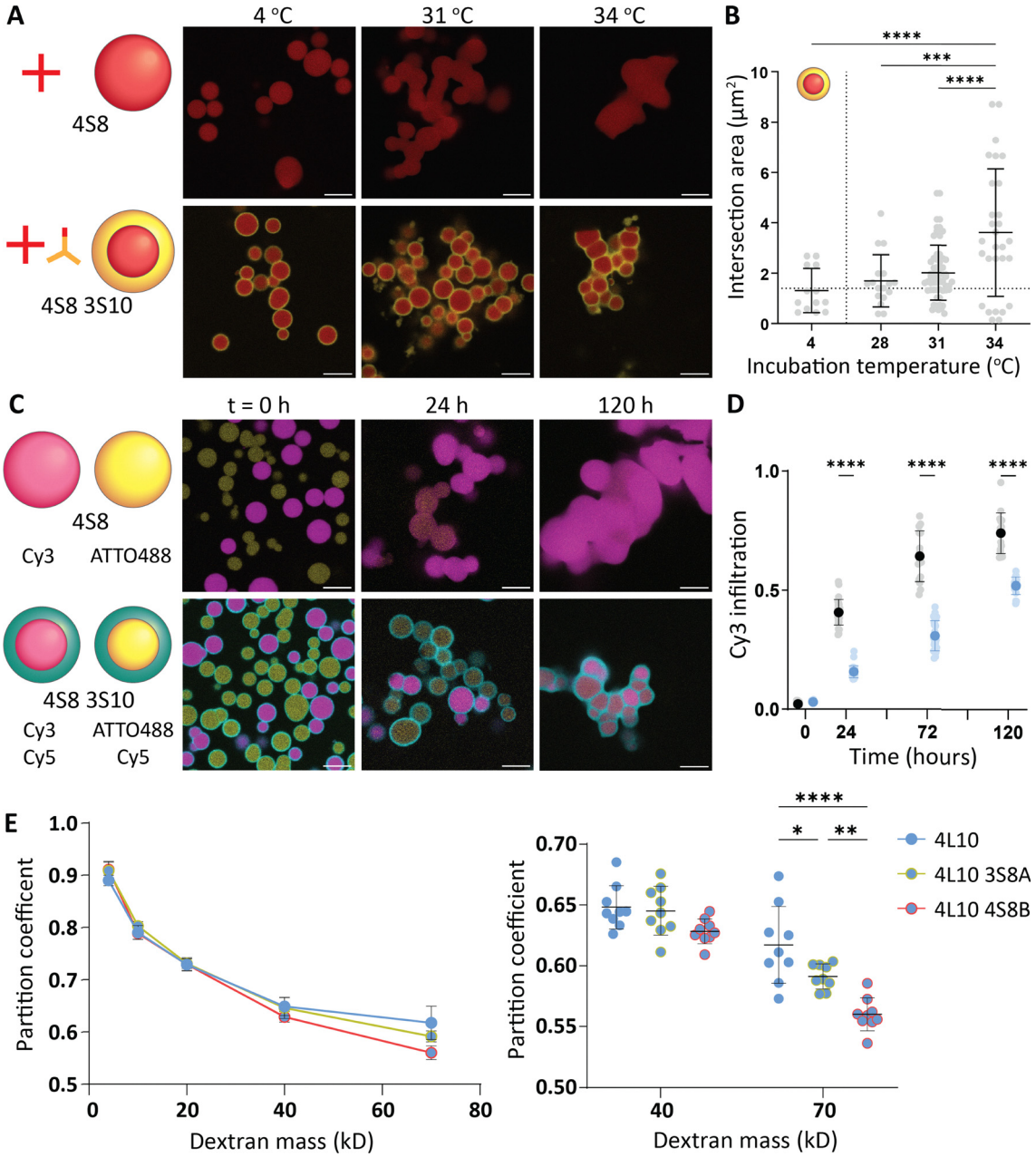

Fig. 5 Core–shell and core-only droplet stability and contents exchange. (A) Core-only droplets fuse rapidly leading to nonuniform populations after 15 hours of incubation (4S8, 31 °C). Core–shell droplets remain stable at this temperature (4S8 3S10). Above 31 °C, shells become more liquid and merge, but cores remain distinct. (B) Areas of intersection for 4S8 3S10 droplets incubated at a range of temperatures for 15 h. Line at $y = 1.4\ \mu m^2$ indicates mean area of intersection in samples immediately following annealing. A significant increase in area mean and range is seen at 34 °C, indicating deformation of shells. (C) Droplets with different core labels were separately annealed then mixed. After incubation at 28 °C for 120 h, core-only 4S8 droplets fuse into extended aggregates. Core–shell 4S8 3S10 droplets merge into extended structures, with individual core–shell regions deformed but distinguishable. (D) Degree of Cy3 core label infiltration in ATTO488 core regions for core-only (black) and core–shell droplets (blue). (E) Partitioning of dextran cargo to the core (4L10) for core-only and core–shell droplets (4L10 3S8-strong, 4L10 4S8-weak), showing significant reduction for core–shell with largest reduction for the 4S shell, which has smallest mesh size. Partitioning is most significant for largest dextran size. Scale bars 10 μm.

The transfer of DNA nanostar components between dilute (solution) and dense (droplet) phases was then compared between core-only and core–shell droplets over time. Two 4S8 core-only droplet populations, differing only in the core fluorophore label (Cy3 or ATTO488), were prepared separately, mixed, then incubated at 28 °C and observed over time. Similarly, two core–shell 4S8 3S10 droplet populations with different core labels were prepared, mixed, and observed during incubation (Fig. 5C). The degree of Cy3 fluorescence infiltration into ATTO488 core regions increased with time for both core-only and core–shell droplets, indicating exchange of contents between discrete cores or core and dilute phases.

However, infiltration was significantly higher for core-only droplets as compared to core–shell droplets at all time points (Fig. 5D). Core–shell droplets were seen to qualitatively retain spherical shapes, with slight deformation. Over the same time period, core-only droplets merged into large extended structures with little distinction between individual droplets.

Cargo partitioning into the core was then directly tested for core–shell droplets by dextran infiltration, and compared for 4L10 as core-only, or with 2 possible shells (3S8-strong, 4S8-weak). In single-phase data, 4S8-weak stars had lower permeability for higher MW dextran than either 4L10 or 3S8-strong (Fig. S7). Similarly, a small but statistically significant decrease in the partition coefficient was observed for 4L10 4S8-weak droplets in comparison to 4L10 (Tukey multiple comparisons, $P = 0.0015$) and 4L10 3S8-strong droplets ($P = 0.0005$) (Fig. 5E), particularly for Dextran mass of 70 kD. This indicated a decrease in the rate of dextran infiltration through the 4S8-weak shell.

Discussion

Here we present a new method for assembly of multi-phase core–shell DNA micro-droplets suitable for use as synthetic microreactors, with control over size, distribution, stability, and permeability. This was achieved by systematic variation of DNA nanostar designs, allowing for wider sampling of droplet properties in two-phase systems than in previous work. The formation of core–shell microarchitecture was found to strongly depend on the relative thermodynamic properties of the component nanostars and was found to be largely independent of nanostar subunit size for the size range tested, allowing for selective tuning of the nano-scale mesh densities in each region.

Initial investigations quantified the size and polydispersity of bare core-only droplets from confocal images (Fig. S2 and S4). Some droplet populations had bimodal size distributions, in visual agreement with typical images (Fig. S1). While previous work has characterised mean droplet size and average growth of DNA nanostar droplet populations over time, there is little available information on size distributions.[18] Observed size distributions of droplets at the coverslip interface may be affected by DNA concentration, surface interactions, temperature gradients in the imaging chamber, or imaging and analysis parameters. Interestingly, bimodal size distributions have also recently been observed in protein condensates in solution by holographic microscopy, but mechanisms are unknown.[51] We have further shown that single phase droplets can differ in physical properties such as size, nanostar mobility, and mesh size (SI). Thus, two phase droplets provide potential for two zones of distinct physical properties.

Our results demonstrate that the difference in phase separation temperature (ΔT_{PS}) of the two phases is an important factor in which phase forms the core in core–shell droplets. This is in contrast to the size-based de-mixing observed in other systems.[22,49] This suggests a kinetic method of core–shell formation, where higher T_{PS} core nanostars initially undergo phase separation at high temperatures (Fig. 1C). Later, when the lower T_{PS} shell stars begin to phase separate, their partial complementarity to the extant droplets allows them to nucleate upon the droplet surface, forming a continuous shell.[52] Our results suggest that after annealing the droplets are kinetically trapped in this morphology and further rearrangement does not occur (Fig. 4B), similar to previous work on coacervation of extended DNA polymers.[21] Interestingly, over longer time scales smaller stars with more dense phases did not migrate to the centre of a droplet to form a core, and more liquid-like cores did not escape to the shell. Thus, we determined that selection of star combinations with appropriate differences in phase separation temperature is important when designing core–shell systems.

Future exploration in this area may include variations in nanostar structure and increased sticky end lengths. Increasing valency and determining the %C required for core–shell formation would help quantify interfacial tensions. Increasing SE length would provide a greater range of T_{PS}, but may result in increased hairpin formation in the palindromic sticky ends.[45] The experimentally-derived T_{PS} used were measured using hybridisation curve analysis for droplet cooling during annealing. Earlier HCA analysis of the assembly of DNA origami and individual DNA nanostars demonstrated hysteresis between melting and cooling curves, attributed to cooperativity.[22,46] Future exploration of cooling and heating differences for nanostar droplets could provide insight into the role of cooperativity in these systems.

Importantly, core–shell DNA droplets were more uniform and stable over time than core-only droplets, which are essential properties for assembly of microreactor systems. Droplet growth in phase separated DNA nanostar systems occurs partially through fusion, a random process that leads to increase in size and size distribution with increase of time spent in the active range during annealing ($T_{PS} - T_G$). We propose that in our systems the shell can act as a steric block, preventing cores from fusing at temperatures between T_{PS}-B and T_G-A, thus shortening the active range of the star A core. Thus, addition of a shell was successfully shown to achieve more uniform droplet populations of well-defined size, and ramp rate was used to tune core size and shell thickness.

Despite the increased stability, the core–shell droplet systems retain important dynamic properties required for microreactors. Individual nanostars are observed to infiltrate cores, either from the dilute phase or from one core to another. We demonstrate that the physical properties of the membrane-like shell have the ability to regulate both the rate of passive cargo infiltration to the core, as well as the rate of specific nanostar infiltration into the core. This property is key when designing synthetic cells or microreactors, as it suggests the infiltration or capture of cargo molecules would be possible if functionalised with appropriate ssDNA sequences. Nanostar infiltration is significantly reduced by the shell. Bare droplets have an 18-fold increase in infiltrated DNA in 24 h, whereas layered droplets have a 5-fold increase. This could be relevant for applications in DNA strand displacement amplification, where nanostar infiltration would correspond to signal leakage. In comparison, movement of contents in and out of synthetic cells or microreactors formed using lipid

vesicles require more complex transport mechanisms such as transmembrane pores.[27]

Future directions include the development of DNA nanostar droplets with even greater complexity, allowing for the creation of synthetic cells or micro-reactors with increased dynamic functions, as well as enhanced understanding of multi-phase cellular coacervates. Overall, the addition of an outer shell provides DNA nanostar microdroplets with essential key features and opens new avenues for exploring increasingly complex artificial systems, such as microreactors and synthetic cells. Importantly, all the interactions in these multi-phase DNA droplets are achieved through canonical DNA hybridisation. Thus, all the specificity and dynamic control of DNA can be exploited in these synthetic systems. We envision that core–shell DNA droplets will enable future dynamic functions. DNA strand displacement could achieve dynamic modification of both core and shell properties after formation, such as removal of the outer shell, triggered transition between low and high deformability of the core while the shell maintains a distinct compartment, or adaptive modification of shell permeability in response to external signals using DNA circuits triggered by light or pH.

Materials and methods

Nanostar design

Three sets of DNA nanostar sequences were designed using NUPACK[44] software, based on previously published nanostar structural motifs.[16,17,42] All arm sequences and SE variant sequences were designed to be orthogonal and designed have no cross-interaction (Tables S1 and S2). 'Surfactant' stars are formed by swapping an arm's SE sequence for a SE from another star (*e.g.* 6 to 8), to produce a new hybrid star with a mix of SEs (*e.g.* 6 and 8) that crosslinks the two original stars.

Oligonucleotides

All oligonucleotides were purchased from IDT DNA Singapore. Unmodified strands were purified by desalting technique during manufacturing. Fluorophore-modified strands were purchased purified by high-performance liquid chromatography (HPLC). Oligonucleotides were dissolved in ultrapure water (MilliQ) to a concentration of 55 μM and stored at 4 °C until use.

Droplet preparation

Star arm strands were combined to a final concentration of 10 μM DNA each, in a solution containing 0.5 M NaCl. Connector and fluorophore-modified strands were added at 1% molar concentration. The resultant solutions were heated in a PCR thermocycler (Applied Biosystems ProfFlex PCR) for 15 minutes at 95 °C and annealed from 95 °C to 5 °C at a rate of −0.5 °C min^{-1}, unless otherwise stated. Following annealing, the resulting solution was pipetted into a viewing chamber, a 2 mm channel prepared from melted Parafilm® between a white glass microscope slide and #1.5 coverslip. Prior to assembly, each slide was cleaned *via* sonication for five minutes each in propanol and MilliQ water, followed by drying under pressurised air or nitrogen gas. The ends of the chamber were then sealed using a two-part epoxy resin, to reduce evaporation.

Droplet imaging

Sample imaging was performed on a Leica TCS SP8 Multiphoton Microscope, with a white light laser and HyD and PMT detectors, with 93× glycerol objective. Excitation and emission wavelengths used were: Cy 3 550/560–620 nm, Cy5 640/650–720 nm, FITC 488/500–540 nm, ATTO488 488/500–540 nm. Images were collected at 1024 × 1024 resolution at 400 Hz and captured as z-stack of 14 μm height and converted to z-projection for analysis. For multiple fluorophores scanning was conducted sequentially. For morphology analysis 20 frame time series were captured and summed. Droplet size was measured using MATLAB function imfindcircles, applying a Circular Hough Transformation. To avoid false positive droplet detection, regions were discarded if mean region intensity was $<1.5\times$ the total average image intensity.

Dynamic light scattering

DLS was conducted on 0 SE stars formed under standard conditions using a Zetasizer Ultra (Malvern Panalytical, Australia). The parameters used were a refractive index of 1.5826 and an extinction coefficient of 0.00. All measurements were conducted at 25 °C using 500 μL of sample and were repeated in triplicate.

Fluorescence recovery after photobleaching

FRAP was conducted Using a LEICA TCS SP5 with 561 nm excitation laser and 571–621 nm emission and 100× oil immersion objective. Samples were heated using a LAUDA Ecoline RE 206 water-heated stage for 20 min prior to imaging. Five consecutive baseline frames were captured pre-bleaching. Regions of interest were irradiated at 70% laser power for 30 seconds. Recovery was captured for five minutes at 3 s $frame^{-1}$. Images were analysed using ImageJ. ROI were manually identified, and pixel intensity data extracted using plugin Create Spectrum JRU v1.[53] Raw data was then processed to account for photofading and normalised against a reference droplet using published methods.[54]

Dextran partitioning

4–70 kD Dextran molecules functionalised with fluorophore (FITC, Sigma Aldrich, Australia), were added to 8, 8-strong, and 10 nt SE droplets at 50 μg mL^{-1}. Solutions were mixed and incubated for 10 hours at 4 °C then imaged using a LEICA SP5 confocal microscope, with excitation/emission 488/500–540 nm. Images were captured as a series of twenty sequential frames and summed. Droplets were manually selected and fluorescence intensity (FITC) was compared between droplet and bulk solution (n = 9 per sample) to calculate partition coefficient of FITC-dextran.

Hybridisation curve analysis

HCA[46] was conducted using a RotorGene Q Real-Time PCR System (Qiagen, Germany). DNA solutions (10 μM nanostructures, 500 mM NaCl) were prepared without fluorophore strands, and 0.1× qPCRBIO SyGreen Lo-ROX Blue Master Mix (PCR Biosystems, UK) was added. Samples were heated to 95 °C for five minutes, then cooled at −0.5 °C min^{-1} to 25 °C. Fluorescence was measured every 60s with excitation/emission 470 ± 10/510 ± 5 nm for $n = 4$ repeats. Data was normalised to 0–100% fluorescence intensity. The resulting fluorescence intensity curves were analysed to identify the temperature of phase separation by dips in fluorescence.

Conflicts of interest

There are no conflicts to declare.

Data availability

All data relevant to this article have been included in the associated supplementary information (SI). Supplementary information is available. See DOI: https://doi.org/10.1039/d5nh00788g.

Acknowledgements

The authors acknowledge funding from: the Australian Research Council (ARC): DP220101528; Westpac Research Fellowship (S.W.); The University of Sydney and The University of Sydney Nano Institute (K.S.); The L E R Tonnet and Family Scholarship in Chemistry (K.S.). The authors acknowledge the facilities as well as the scientific and technical assistance of the Australian Microscopy & Microanalysis Research Facility (ammrf.org.au) node at the University of Sydney: Sydney Microscopy & Microanalysis, and Sydney Analytical, a core research facility at the University of Sydney.

References

1 C. P. Brangwynne, *et al.*, Germline P Granules Are Liquid Droplets That Localize by Controlled Dissolution/Condensation, *Science*, 2009, **324**, 1729–1732.
2 A. A. Hyman, C. A. Weber and F. Jülicher, Liquid-Liquid Phase Separation in Biology, *Annu. Rev. Cell Dev. Biol.*, 2014, **30**, 39–58.
3 B. Wang, *et al.*, Liquid–liquid phase separation in human health and diseases, *Signal Transduction Targeted Ther.*, 2021, **6**, 290.
4 M. Abbas, J. O. Law, S. N. Grellscheid, W. T. S. Huck and E. Spruijt, Peptide-Based Coacervate-Core Vesicles with Semipermeable Membranes, *Adv. Mater.*, 2022, **34**, 2202913.
5 L. Jiang, *et al.*, Peptide-Based Coacervate Protocells with Cytoprotective Metal–Phenolic Network Membranes, *J. Am. Chem. Soc.*, 2023, **145**, 24108–24115.
6 A. F. Mason, B. C. Buddingh, D. S. Williams and J. C. M. van Hest, Hierarchical Self-Assembly of a Copolymer-Stabilized Coacervate Protocell, *J. Am. Chem. Soc.*, 2017, **139**, 17309–17312.
7 S. Alberti, A. Gladfelter and T. Mittag, Considerations and Challenges in Studying Liquid-Liquid Phase Separation and Biomolecular Condensates, *Cell*, 2019, **176**, 419–434.
8 J. Li, X. Liu, L. K. E. A. Abdelmohsen, D. S. Williams and X. Huang, Spatial Organization in Proteinaceous Membrane-Stabilized Coacervate Protocells, *Small*, 2019, **15**, 1902893.
9 G. A. Mountain and C. D. Keating, Formation of Multiphase Complex Coacervates and Partitioning of Biomolecules within them, *Biomacromolecules*, 2020, **21**, 630–640.
10 A. P. Constantinou, A. Tall, Q. Li and T. K. Georgiou, Liquid–liquid phase separation in aqueous solutions of poly(ethylene glycol) methacrylate homopolymers, *J. Polym. Sci.*, 2022, **60**, 188–198.
11 T. Mashima, *et al.*, DNA-Mediated Protein Shuttling between Coacervate-Based Artificial Cells, *Angew. Chem., Int. Ed.*, 2022, **61**, e202115041.
12 K. Matsuura, T. Yamashita, Y. Igami and N. Kimizuka, 'Nucleo-nanocages': designed ternary oligodeoxyribonucleotides spontaneously form nanosized DNA cages, *Chem. Commun.*, 2003, 376–377, DOI: 10.1039/b210139d.
13 B. Jeon, *et al.*, Salt-dependent properties of a coacervate-like, self-assembled DNA liquid, *Soft Matter*, 2018, **14**, 7009–7015.
14 D. T. Nguyen, B. Jeon, G. R. Abraham and O. A. Saleh, Length-Dependence and Spatial Structure of DNA Partitioning into a DNA Liquid, *Langmuir*, 2019, **35**, 14849–14854.
15 O. A. Saleh, B. Jeon and T. Liedl, Enzymatic degradation of liquid droplets of DNA is modulated near the phase boundary, *Proc. Natl. Acad. Sci. U. S. A.*, 2020, **117**, 16160–16166.
16 B. Jeon, D. T. Nguyen and O. A. Saleh, Sequence-Controlled Adhesion and Microemulsification in a Two-Phase System of DNA Liquid Droplets, *J. Phys. Chem. B*, 2020, **124**, 8888–8895.
17 Y. Sato, T. Sakamoto and M. Takinoue, Sequence-based engineering of dynamic functions of micrometer-sized DNA droplets, *Sci. Adv.*, 2020, **6**, eaba3471.
18 S. Agarwal, D. Osmanovic, M. A. Klocke and E. Franco, The Growth Rate of DNA Condensate Droplets Increases with the Size of Participating Subunits, *ACS Nano*, 2022, **16**, 11842–11851.
19 H. Udono, J. Gong, Y. Sato and M. Takinoue, DNA Droplets: Intelligent, Dynamic Fluid, *Adv. Biol.*, 2022, 2200180, DOI: 10.1002/adbi.202200180.
20 J. Zeng, *et al.*, Self-Assembly of Microparticles by Supramolecular Homopolymerization of One Component DNA Molecule, *Small*, 2019, **15**, 1805552.
21 R. Merindol, S. Loescher, A. Samanta and A. Walther, Pathway-controlled formation of mesostructured all-DNA colloids and superstructures, *Nat. Nanotechnol.*, 2018, **13**, 730–738.
22 M. Walczak, *et al.*, Responsive core-shell DNA particles trigger lipid-membrane disruption and bacteria entrapment, *Nat. Commun.*, 2021, **12**, 4743.
23 S. Do, C. Lee, T. Lee, D.-N. Kim and Y. Shin, Engineering DNA-based synthetic condensates with programmable

material properties, compositions, and functionalities, *Sci. Adv.*, 2022, **8**, eabj1771.
24 M. Michel, *et al.*, Giant Liposome Microreactors for Controlled Production of Calcium Phosphate Crystals, *Langmuir*, 2004, **20**, 6127–6133.
25 P.-Y. Bolinger, D. Stamou and H. Vogel, Integrated Nanoreactor Systems: Triggering the Release and Mixing of Compounds Inside Single Vesicles, *J. Am. Chem. Soc.*, 2004, **126**, 8594–8595.
26 J. W. Hindley, *et al.*, Light-triggered enzymatic reactions in nested vesicle reactors, *Nat. Commun.*, 2018, **9**, 1093.
27 Y. Elani, R. V. Law and O. Ces, Vesicle-based artificial cells as chemical microreactors with spatially segregated reaction pathways, *Nat. Commun.*, 2014, **5**, 5305.
28 Q. Xu, *et al.*, Preparation and biomedical applications of artificial cells, *Mater. Today Bio*, 2023, **23**, 100877.
29 W. Mu, *et al.*, Superstructural ordering in self-sorting coacervate-based protocell networks, *Nat. Chem.*, 2024, **16**, 158–167.
30 E. Kengmana, E. Ornelas-Gatdula, K.-L. Chen and R. Schulman, Spatial Control over Reactions via Localized Transcription within Membraneless DNA Nanostar Droplets, *J. Am. Chem. Soc.*, 2024, **146**, 32942–32952.
31 J. Bucci, *et al.*, Enzyme-Responsive DNA Condensates, *J. Am. Chem. Soc.*, 2024, **146**, 31529–31537.
32 D. T. Nguyen and O. A. Saleh, Tuning phase and aging of DNA hydrogels through molecular design, *Soft Matter*, 2017, **13**, 5421–5427.
33 N. Conrad, G. Chang, D. K. Fygenson and O. A. Saleh, Emulsion imaging of a DNA nanostar condensate phase diagram reveals valence and electrostatic effects, *J. Chem. Phys.*, 2022, **157**, 234203.
34 A. Leathers, *et al.*, Reaction–Diffusion Patterning of DNA-Based Artificial Cells, *J. Am. Chem. Soc.*, 2022, **144**, 17468–17476.
35 S. Do, C. Lee, T. Lee, D.-N. Kim and Y. Shin, Engineering DNA-based synthetic condensates with programmable material properties, compositions, and functionalities, *Sci. Adv.*, 2022, **8**, eabj1771.
36 M. P. Tran, *et al.*, A DNA Segregation Module for Synthetic Cells, *Small*, 2023, **19**, 2202711.
37 N. Yamashita, Y. Sato, Y. Suzuki, D. Ishikawa and M. Takinoue, DNA-Origami-Armored DNA Condensates, *ChemBioChem*, 2024, **25**, e202400468.
38 D. Y. Zhang and E. Winfree, Control of DNA Strand Displacement Kinetics Using Toehold Exchange, *J. Am. Chem. Soc.*, 2009, **131**, 17303–17314.
39 T. Z. Jia, C. Hentrich and J. W. Szostak, Rapid RNA Exchange in Aqueous Two-Phase System and Coacervate Droplets, *Origins Life Evol. Biospheres*, 2014, **44**, 1–12.
40 D. Gao, *et al.*, Controlling the size and adhesion of DNA droplets using surface- enriched DNA molecules, *Soft Matter*, 2024, **20**, 1275–1281.
41 C. C. M. Sproncken, B. Gumí-Audenis, S. Foroutanparsa, J. R. Magana and I. K. Voets, Controlling the Formation of Polyelectrolyte Complex Nanoparticles Using Programmable pH Reactions, *Macromolecules*, 2022, **56**, 226–233.
42 S. Biffi, *et al.*, Phase behavior and critical activated dynamics of limited-valence DNA nanostars, *Proc. Natl. Acad. Sci. U. S. A.*, 2013, **110**, 15633–15637.
43 J. SantaLucia, A unified view of polymer, dumbbell, and oligonucleotide DNA nearest-neighbor thermodynamics, *Proc. Natl. Acad. Sci. U. S. A.*, 1998, **95**, 1460–1465.
44 J. N. Zadeh, *et al.*, NUPACK: Analysis and design of nucleic acid systems, *J. Comput. Chem.*, 2011, **32**, 170–173.
45 Y. Sato and M. Takinoue, Sequence-dependent fusion dynamics and physical properties of DNA droplets, *Nanoscale Adv.*, 2023, **5**, 1919–1925.
46 J.-P. J. Sobczak, T. G. Martin, T. Gerling and H. Dietz, Rapid Folding of DNA into Nanoscale Shapes at Constant Temperature, *Science*, 2012, **338**, 1458–1461.
47 C. Li, L. Meng, Y. Tong, J. Lin and Z. Qi, Hollow condensates emerge from gelation-induced spinodal decomposition, *Proc. Natl. Acad. Sci. U. S. A.*, 2025, **122**, e2520491122.
48 D. A. Tanase, *et al.*, Internal Phase Separation in Synthetic DNA Condensates, *Adv. Sci.*, 2025, **12**, e06275.
49 L. Malouf, *et al.*, Sculpting DNA-based synthetic cells through phase separation and phase-targeted activity, *Chem*, 2023, **9**, 3347–3364.
50 K. Matsuura, K. Masumoto, Y. Igami, T. Fujioka and N. Kimizuka, In Situ Observation of Spherical DNA Assembly in Water and the Controlled Release of Bound Dyes, *Biomacromolecules*, 2007, **8**, 2726–2732.
51 J. von Hofe, *et al.*, Multivalency Controls the Growth and Dynamics of a Biomolecular Condensate, *J. Am. Chem. Soc.*, 2025, **147**, 25242–25253.
52 C. Y. G. Lemetter, F. M. Meeuse and N. J. Zuidam, Control of the morphology and the size of complex coacervate microcapsules during scale-up, *AIChE J.*, 2009, **55**, 1487–1496.
53 J. Unruh Create Spectrum JRU v1. Stowers Institute for Medical Research (2010).
54 I. Alshareedah, T. Kaur and P. R. Banerjee, Methods for Characterizing the Material Properties of Biomolecular Condensates, *Methods Enzymol.*, 2021, **646**, 143–183.

